

Article

High-Energy and High-Power Primary Li-CF_x Batteries Enabled by the Combined Effects of the Binder and the Electrolyte

Haobin Huo ¹, Sivaviswa Radhakrishnan ¹, Leon L. Shaw ¹ and Károly Németh ^{2,*}

¹ Mechanical, Materials and Aerospace Engineering Department, Illinois Institute of Technology, 10 W. 32nd St., Chicago, IL 60616, USA; hhuo2@hawk.iit.edu (H.H.); sradhakrishnan1@hawk.iit.edu (S.R.); lshaw2@iit.edu (L.L.S.)

² Physics Department, Illinois Institute of Technology, 3101 South Dearborn St., Chicago, IL 60616, USA

* Correspondence: knemeth@iit.edu

Abstract: Several effective methods have been developed recently to demonstrate simultaneous high energy and high power density in Lithium - carbon fluoride (Li-CF_x) batteries. These methods can achieve as high as a 1000 Wh/kg energy density at a 60–70 kW/kg power density (40–50 C rate) in coin cells and a 750 Wh/kg energy density at a 12.5 kW/kg power density (20 C rate) in pouch cells. This performance is made possible by an ingenious nano-architecture design, controlled porosity, boron doping, and electrolyte additives. In the present study, we show that a similarly great performance, a 931 Wh/kg energy density at a 59 kW/kg power density, can be achieved by using a polyacrylonitrile binder and a LiBF₄ electrolyte in Li-graphite fluoride coin cells. We also demonstrate that the observed effect is the result of the right combination of the binder and the electrolyte. We propose that the mechanistic origin of the observed phenomena is an electro-catalytic effect of the polyacrylonitrile binder. While our proposed method has a competitive performance, it also offers a simple implementation and a scalable production of high-energy and high-power primary Li-CF_x cells.

Keywords: graphite fluoride; battery; polyacrylonitrile; lithium fluoride; nucleation; crystal growth



Citation: Huo, H.; Radhakrishnan, S.; Shaw, L.L.; Németh, K. High-Energy and High-Power Primary Li-CF_x Batteries Enabled by the Combined Effects of the Binder and the Electrolyte. *Batteries* **2023**, *9*, 268. <https://doi.org/10.3390/batteries9050268>

Academic Editors: Pascal Venet, Karim Zaghib and Seung-Wan Song

Received: 26 March 2023

Revised: 6 May 2023

Accepted: 9 May 2023

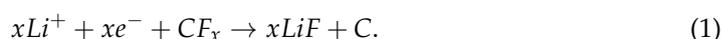
Published: 12 May 2023



Copyright: © 2023 by the authors. Licensee MDPI, Basel, Switzerland. This article is an open access article distributed under the terms and conditions of the Creative Commons Attribution (CC BY) license (<https://creativecommons.org/licenses/by/4.0/>).

1. Introduction

Functionalized two-dimensional (2D) materials as cathode active species have a demonstrated ability to realize simultaneously high energy and high power in primary and secondary batteries. These features are highly desirable for many applications ranging from electric cars to electric aircraft, space exploration, pulsed power sources, and medical devices [1–7]. Graphite fluoride (CF_x, 0 < x < 1.3) is the oldest-known example of functionalized 2D materials as cathode active species. The structure of fully fluorinated graphite has been known since 1947 and consists of stacked fluorinated layers of graphene [8,9]. The Li-CF_x primary battery was commercialized in 1970 [10–12]. It offers many advantages such as a high energy and high power density, excellent shelf-life, applicability in a wide temperature range (–60 to +60 °C), and a relatively easy-to-source and economic composition [13–17]. It has a very high theoretical specific energy of 2180 Wh/kg at a capacity of 864 mAh/g when graphite is fully fluorinated (x ≈ 1) and an open circuit voltage (OCV) of 3.2–3.3 V [10]. It is a primary battery with only a limited degree of rechargeability [18,19]. The cell reaction on discharge is the following:



If the discharge product carbon would be graphite, an OCV of 4.57 V should be observed on the basis of thermodynamics calculations [20,21]. The much lower observed OCV is a consequence of the formation of the sandwich structure of LiF and graphene in the discharge product [20–22].

The study of solvent effects has led to the recognition that the solvated Li^+ ion intercalates between the stacked CF_x monolayers during discharge, and the solid LiF discharge product forms only after the collapse of the solvent shell of Li^+ between the CF_x layers [21,22]. The higher the solvation energy of Li^+ in a given solvent, the lower the discharge voltage is [22].

The intercalation of solvated Li^+ ions was also seen in graphene oxide (GO) cathodes. In order to achieve a high power density in Li/Na -GO batteries, the GO interlayer distance must be expanded, which is typically achieved via a thermal treatment of GO before building the cathode [23–27]. The layer distance in fully fluorinated CF_x is about 6–9 Å [9], and the interaction between the layers is weak enough to allow for the penetration of some solvated Li^+ ions. The discharged CF_x (which includes the intercalated CF_x and its discharge products) typically forms a shell around a core of CF_x particles and has a major impact on the overall performance of the Li - CF_x cells [28]. The time evolution of the structure and composition of the cathode during discharge was studied recently in detail at a slow discharge [29]. As opposed to the expectations, the graphene layers transform into a hard carbon structure during discharge with a much reduced sp^2 carbon content. The optimization of the structure and composition of the domain of the discharged CF_x is the key to improving the electrochemical performance of Li - CF_x cells.

The specific power of Li - CF_x cells used to be small historically. In 2007, commercial Li - CF_x batteries were reported to have a break-down of specific energy at a specific power of ≈ 1.6 kW/kg, which was cured by the introduction of partially fluorinated CF_x ($\approx 0.3 < x < \approx 0.8$) cathodes. Partially fluorinated CF_x could realize much higher specific power values and a break-down of specific energy at 10 kW/kg [30,31]. Research on high-power Li - CF_x batteries intensified in the past decade. Various approaches have been developed that are capable of delivering a specific energy of 800–1000 Wh/kg at power densities of 20–70 kW/kg (15–50 C rates). These approaches utilize a nano-architecture design, such as fluorinated graphene microspheres [32], increased porosity and edge (instead of in-plane) functionalization [33–36], and amorphization of the discharge product LiF [37]. Recently, the amorphization of LiF was achieved by the addition of BF_3 gas in the electrolyte at a 0.01 M concentration and was confirmed by the lack of the LiF pattern in the X-ray diffraction pattern of the discharged CF_x cathode [37]. The amorphization of LiF was also observed when a solid electrolyte, Li_3PS_4 , was used [38].

Another method of the amorphization of the discharge product LiF was proposed by Jones and Hossain about a decade ago as a way to reduce the relatively high heat production during discharge [39]. These inventors proposed using polymeric binders that serve a dual purpose: (1) they mechanically bind the components of the cathode together and (2) act as the complexation/amorphization agents of LiF . Several such polymers were proposed as a replacement for the more traditional poly(vinylidene difluoride) (PVDF) and Teflon (PTFE), among them polyacrylonitrile (PAN) derivatives (primarily complexing the Li^+ ions) and boronates (primarily complexing F^- ions). These complexation phenomena are typically based on Lewis acid–base reactions. The gaseous BF_3 electrolyte additive mentioned above is a simple example of the formation of a Lewis adduct of LiF with BF_3 as BF_3 is well known to easily dissolve LiF in the form of LiBF_4 . Unfortunately, the theoretical proposal of Jones and Hossain has not been experimentally demonstrated to date, to the best of our knowledge.

We have been working on the development of high-energy and high-power batteries based on functionalized 2D materials for about a decade [40–45]. We recently proposed the use of adducts of BF_3 with graphene oxide (GO) and oxidized hexagonal boron nitride (hBN) as cathode active species and solid electrolytes [42–45].

The above-mentioned successful application of the BF_3 gas additive in Li - CF_x cells [37] called our attention to the role of BF_3 and its adducts in high-power Li - CF_x cells. However, our initial attempt to use BF_3 -etherate as a safer alternative to BF_3 gas in Li - CF_x cells to achieve high power density failed. This motivated us to investigate alternatives. We explored the use of $\text{LiOX}\cdot\text{BF}_3$ ($X = \text{Li}, \text{H}$) to substitute $-\text{F}$ with $-\text{OBF}_3$ groups in CF_x for a

greater interlayer spacing. As the addition of $\text{LiOX}\cdot\text{BF}_3$ led to an alkaline cathode, we also investigated a PAN binder instead of the traditional PVDF because the latter one is not stable in an alkaline environment [46]. This study resulted in the discovery of the beneficial effects of the PAN binder on the power density of Li-CF_x cells. Furthermore, we also discovered that such a binder effect occurs only in select electrolytes. While the mechanistic origin of the combined binder and electrolyte effects is not clear yet, we propose that it is likely related to the electro-catalytic activity of PAN. The details of our findings are described below.

2. Materials and Methods

Graphite fluoride (CF_x) was purchased from ACS Material (Product Number GT1FS012) with the F/C ratio being 0.8–1.1. The X-ray diffraction (XRD) pattern (at $\text{Cu K}\alpha$ X-ray radiation) of this CF_x is shown in Figure 1. The (002) reflection at 26.7 deg indicates the presence of some non-fluorinated graphite species.

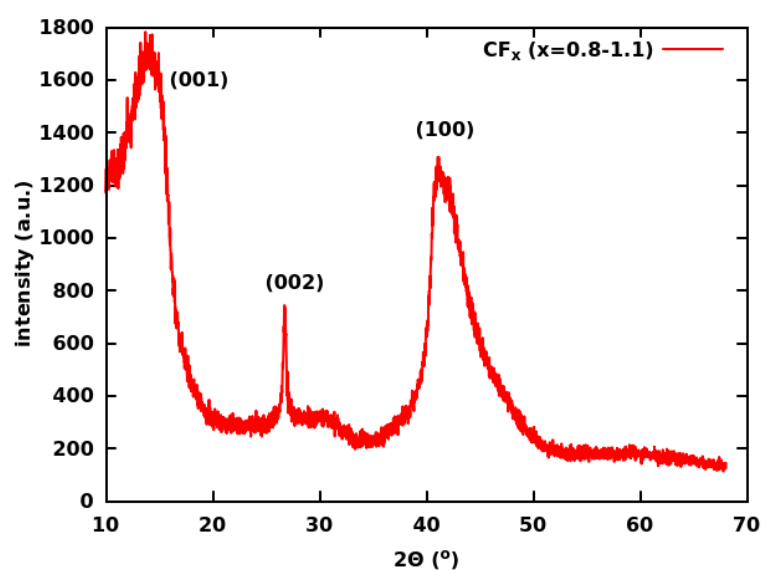


Figure 1. XRD ($\text{Cu K}\alpha$) pattern of the CF_x used in the present study. The presence of some non-fluorinated graphite is indicated by the (002) reflection.

Lithium tetrafluoroborate (LiBF_4), lithium perchlorate (LiClO_4), lithium hexafluorophosphate (LiPF_6), lithium bis(oxalato)borate ($\text{LiB}(\text{C}_2\text{O}_4)_2$ (LiBOB)), polyacrylonitrile (PAN) (average molecular weight 150,000), carbon black (CB), ethylene carbonate (EC), dimethyl carbonate (DMC), propylene carbonate (PC), 1,2 dimethoxy ethane (DME), dimethyl sulfoxide (DMSO), 1,3-dioxalane (DOL), *N,N*-dimethylformamide (DMF), and *N*-Methyl-2-pyrrolidone (NMP) were purchased from Millipore-Sigma. Poly(vinylidene difluoride) (PVDF) was purchased from Alfa Aesar. Conductive carbon black (CB) (TIMCAL Graphite & Carbon Super P) was purchased from MTI Corporation. The as-purchased LiBOB was dried in vacuum at 150 °C for 8 h before use for better solubility in the electrolyte solvents [47].

The cathodes were cast on an Al foil from a slurry using variable spreading gaps (100 and 250 μm). The slurries were made using a mixture of CF_x , binder, and carbon black at a mass ratio of 8:1:1, respectively, unless otherwise noted. The CF_x was ultrasonicated for 4 h in ethanol (EtOH) following similar ultrasonication processes in the literature [48,49] for exfoliation and easier homogenization of the slurry. A Branson Ultrasonics CPX952516R device was used for mild ultrasonication (40 kHz). The binders were added in the form of a 4 w% PAN/DMF or PVDF/NMP solution to the dry solid CF_x and CB and mixed thoroughly in a laboratory mixer (Thinky ARM-310). The cathodes were dried in a vacuum

oven at 120 °C for 8h. A more detailed account of our laboratory procedures is available in [50].

The LiOX·BF₃ additive [51] was synthesized in the presence of CF_x by mixing CF_x with Li₂CO₃ in a 20:1 molar ratio and ultrasonicated the mixture in F₃B·OEt₂ for 4 h. The product was washed with dichloromethane and filtered on a nanoporous filter. The products were dried in vacuum after ultrasonication.

Cathode disks of 0.65 cm in radius were punched out of the cathode sheets and placed into CR2032 coin cell cases. Porous polypropylene disks (Celgard 2500, 25 μm thickness) were used as separators and Li foil disks as anodes. For the electrolyte, a 1 M solution of LiBF₄, LiClO₄, LiPF₆, or LiBOB was used in a 1:1:1 volumetric mixture of the PC, DME, and DOL solvents following a similar electrolyte in [52]. The advantages of using DOL as an electrolyte (co)solvent are discussed in [53], and they in particular include stable artificial solid electrolyte interphase (SEI) formation on lithium metal anodes [54]. Typically, a 60 μL electrolyte was filled in a coin cell. The cells were hermetically sealed using a crimping machine.

The galvanostatic cycling of the coin cell batteries was carried out using a Neware battery tester (maximum voltage 5V, maximum current 50 mA). The voltage limits were 1.5 and 4.6 V, unless otherwise noted. Electrochemical impedance spectra (EIS) were measured using a PARSTAT 4000 instrument between 0.1 Hz and 100 kHz at a 10 mV amplitude. XRD was carried out using a Bruker D2 Phaser device at Cu Kα X-ray radiation (1.5406 Å wavelength). Field emission scanning electron microscopy (FESEM) images and related energy dispersion spectroscopy (EDS) atomic maps were measured using a JEOL JSM-6701F device. The cathodes were washed with DMC and dried before entering the FESEM imaging. Synchrotron XRD (at 0.459063 Å wavelength) was carried out at the Advanced Photon Source at Argonne National Laboratory.

3. Results and Discussion

We tested a series of Li-CF_x cells to understand the binder and electrolyte dependence of the power density. The compositions of these cells are listed in Table 1. The blends of the solvents were obtained by mixing equal volumetric amounts of the components. CF_x was ultrasonicated for 4 h before use, except in the case of H304 (0 h) and H101 (3 h). The active material loading was 1.0–1.5 mg/cm² for 100 μm-thick cathodes and 1.9–2.6 mg/cm² for the 250 μm ones. The concentration of the electrolytes was always 1 M. The molar ratio of CF_x to the LiOX·BF₃ additive (when present) was 10:1.

Table 1. Cathode composition in different groups of cells.

Group ID	Ultrasonication of Solvent	CF _x Additive	Thickness (μm)	Binder	Electrolyte Salt	Electrolyte Solvent
H293	EtOH	-	100	PAN	LiBF ₄	PC:DME:DOL
H314	EtOH	-	250	PAN	LiBF ₄	PC:DME:DOL
H214	EtOH	-	100	PVDF	LiBF ₄	PC:DME:DOL
H321	EtOH	-	250	PVDF	LiBF ₄	PC:DME:DOL
H366	EtOH	-	100	PAN	LiPF ₆	PC:DME:DOL
H371	EtOH	-	100	PAN	LiClO ₄	PC:DME:DOL
H429	EtOH	-	100	PAN	LiBOB	PC:DME:DOL
H101	F ₃ B·OEt ₂	-	100	PVDF	LiBF ₄	PC:DME:DOL
H274	F ₃ B·OEt ₂	LiOX·BF ₃	100	PAN	LiBF ₄	PC:DME:DOL
H304	no ultrasonication		100	PAN	LiBF ₄	PC:DME:DOL
H179	F ₃ B·OEt ₂	LiOX·BF ₃	100	PAN	LiBF ₄	DMSO:DOL
H387	EtOH	-	100	PVDF	LiBF ₄	EC:DMC

The composition of the cells in Table 1 reflects the time evolution of our research toward increasingly high-power Li-CF_x batteries and toward understanding the key factors that control the power density. The higher the number in the cell group ID, the later the composition was explored.

The gravimetric energy vs. power density curves of cells with 100 μm -thick cathodes and 1M LiBF_4 electrolytes are shown in Figure 2. The values are given with respect to the weight of the CF_x in the cathode. These cells differ in the type of the binder (PAN or PVDF) and the preparation of the CF_x active material (ultrasonication duration, solvent, and additive). The C rates of the discharge were between 0.05 and 40.

For a reference Li- CF_x cell of traditional composition, we chose the same cell composition as the one in [37], which investigated the effects of a gaseous BF_3 electrolyte additive. It uses a PVDF binder and a 1 M LiBF_4 electrolyte in EC:DMC(1:1). This configuration (Group H387) was highly inferior in performance to all but one of the cell configurations investigated here.

The best-performing cells were from Group H293. These cells provided the highest energy density at a very high power density and performed consistently better than other cells at a higher than 10 kW/kg power density. The Group H293 cells had a simple composition: their cathodes were composed of CF_x , which was ultrasonicated in EtOH for 4 h, and the binder was PAN; no additive or special solvent (such as $\text{F}_3\text{B}\cdot\text{OEt}_2$) was applied.

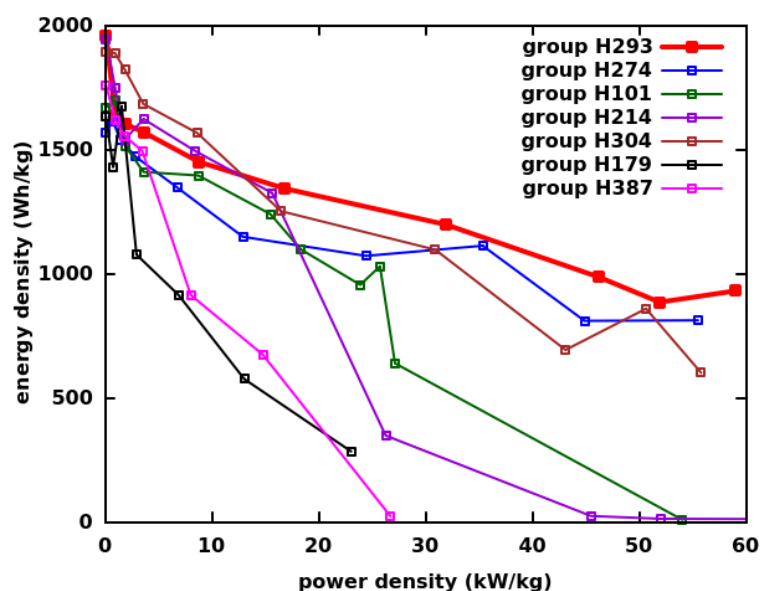


Figure 2. Gravimetric energy density vs. power density of cells containing cathodes with a 100 μm layer thickness. Each cell contained a 1M LiBF_4 electrolyte. The binder was either PAN or PVDF. The detailed composition of the cells can be found in Table 1.

The voltage vs. capacity density curves during the discharge of the Group H293 cells can be seen in Figure 3. They compared very well (especially for high C rates) with similar curves in the best-performing CF_x cells of the literature, such as those in [33–37] and especially those in [32], which we consider to be probably the best-performing CF_x cell demonstrated to date. While the CF_x used in [32] is based on fluorinated graphene microspheres, our method uses the traditional and much-easier-to-synthesize graphite fluoride. Other components of our cathode, such as the PAN binder and the electrolyte (1 M LiBF_4 in PC:DME:DOL(1:1:1)), are also conveniently available. Therefore, our method appears to offer a more economic composition and implementational simplicity, while providing a competitive performance.

Surprisingly, even the as-purchased CF_x (with no ultrasonication, Group H304) allowed for relatively high energy densities at high power densities when used with a PAN binder and LiBF_4 electrolyte. However, when the PAN binder was exchanged with PVDF, the energy density rapidly decayed at high power densities (Group H214). If the CF_x was ultrasonicated in $\text{F}_3\text{B}\cdot\text{OEt}_2$, then the performance became better even if the PVDF binder was used (Group H101); however, it was still greatly inferior to Group H293. This indicates the beneficial effects of BF_3 on the power density similarly to [37]. The ultra-

sonication of CF_x in $\text{F}_3\text{B}\cdot\text{OEt}_2$ with the $\text{LiOX}\cdot\text{BF}_3$ additive (Group H274) did not improve the performance of the simple ultrasonicated CF_x active material when the PAN binder was used. This stresses again the robustness of the Group H293 cathodes. The goal of using the $\text{LiOX}\cdot\text{BF}_3$ additive was to exchange the $-\text{F}$ functional group with $-\text{OBF}_3$ on the surface of the graphene for a greater interlayer distance. A similar reaction between CF_x and NaOH resulted in $-\text{OH}$ functionalized graphene [55], albeit in the presence of a catalyst only. Another reaction between CF_x and NaCN resulted in $-\text{CN}$ functionalized graphene [56] and paracyanogene [57] without a catalyst. The potential of such a metathesis reaction between CF_x and $\text{LiOX}\cdot\text{BF}_3$ is still there, but the reaction conditions should be more carefully investigated.

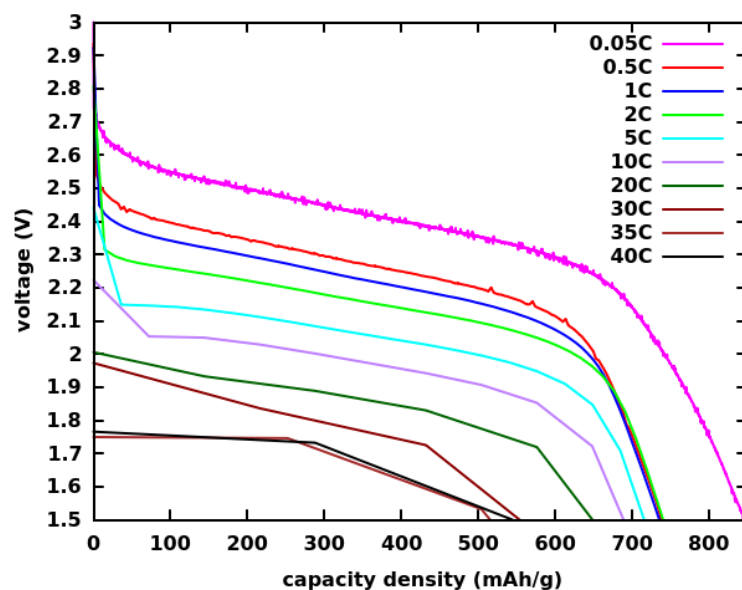


Figure 3. Voltage vs. capacity density curves at various C rates for CF_x batteries in our best-performing cells, which provided the highest energy density at very high power densities (Group H293).

We also explored a 1:1 volumetric mixture of DMSO and DOL as a solvent in a 1M LiBF_4 electrolyte, as it was found in earlier literature that such an electrolyte can raise the discharge voltage [58] at a slow discharge. In our experience, this electrolyte had a poor performance at high C rates (high power density), even when used with a PAN binder (Group H179).

Next, we investigated the effect of the cathode thickness on the performance of the $\text{Li}\text{-CF}_x$ cells while using either the PAN or PVDF binder and keeping the 1 M LiBF_4 electrolyte in $\text{PC:DME:DOL}(1:1:1)$. Two different cathode thickness were used, 100 μm (1.0–1.5 mg/cm^2 CF_x loading) and 250 μm (3.0–4.6 mg/cm^2 CF_x loading). The cathodes with the PAN binder had a greatly superior performance over the cathodes with the PVDF binder at higher power densities (over 10 kW/kg), independent of the cathode thickness, as shown in Figure 4.

In order to learn about the optimal amount of PAN in the cathode, we explored the performance of the cathodes with 5, 10, and 15 w% PAN, while the combined amount of CF_x and PAN was 90 w%. The cathode thickness was 100 μm (about 1.2 mg/cm^2 CF_x loading). The electrolyte was 1 M LiBF_4 in $\text{PC:DME:DOL}(1:1:1)$, as usual. The discharge happened at 0.5, 10, 20, and 30 C rates. The voltage cut-off was 1.5 V. The results are shown in Figure 5. They indicate no clear trends. It seems even 5 w% PAN can provide a great performance. It is likely that the spatial distribution of PAN relative to the CF_x layers and stacks also matters greatly. For a maximum performance enhancement, it may be advantageous to introduce strands of PAN between the exfoliated layers before the

discharge of the battery. In our current slurry-making process, it is more likely that the PAN was mostly attached to the outer surface of the CF_x stacks.

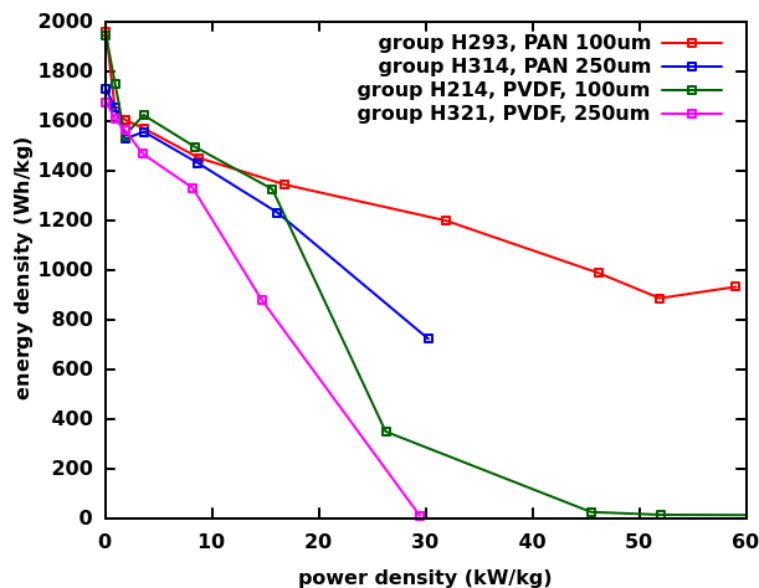


Figure 4. The dependence of the energy vs. power density performance on the type of binder (PAN or PVDF) and on the thickness of the cathode (100 or 250 μm). The electrolyte was 1 M LiBF_4 in PC:DME:DOL(1:1:1).

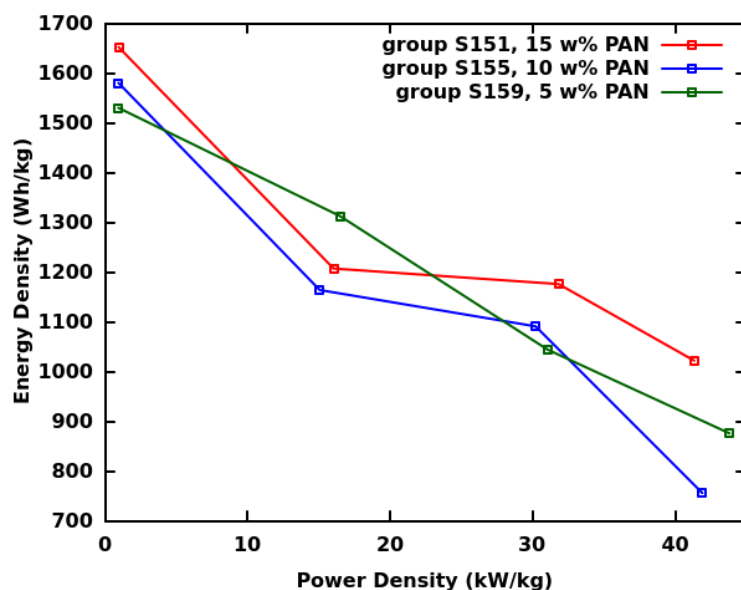


Figure 5. The energy vs. power density performance of Li- CF_x cells with different amounts of PAN in the cathode.

We also explored how the choice of the electrolyte salt influenced the performance of the Li- CF_x cells with the PAN binder. There were 1 M solutions of LiBF_4 , LiClO_4 , LiPF_6 , and LiBOB used in PC:DME:DOL(1:1:1). Figure 6 shows the dependence of the energy vs. power density performance on the type of electrolyte. There was a divergent performance at a greater than 5 kW/kg power density: LiBF_4 performed the best, followed relatively closely by LiClO_4 , while LiPF_6 performed much less well, and LiBOB was by far the slowest discharging one.

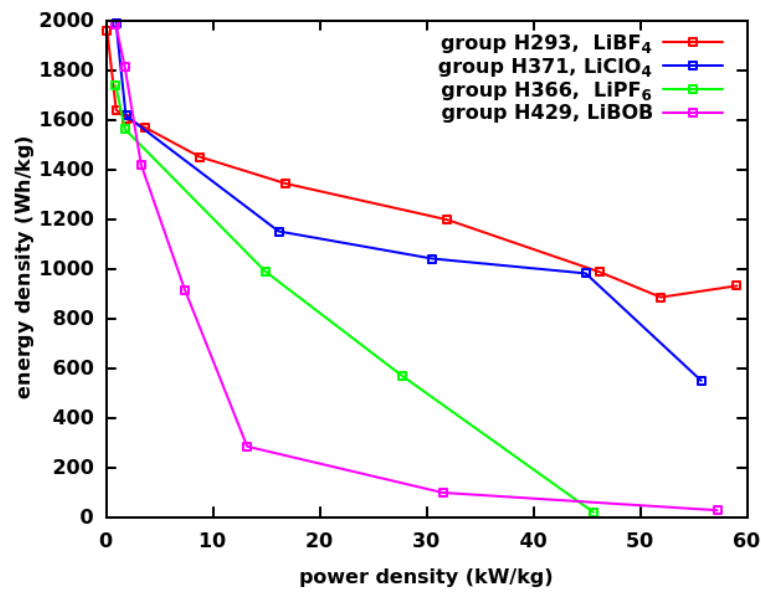


Figure 6. The dependence of the energy vs. power density performance on the type of electrolyte. The effects of LiBF₄, LiClO₄, LiPF₆, and LiBOB electrolyte salts in PC:DME:DOL(1:1:1) solvent were investigated. The cathode thickness was approximately 100 μm in all cases.

Figure 7 shows the impedances (Z) of the electrolytes before (Panel a) and 1 h after (Panel b) full discharge at a 0.5 C rate. The higher-frequency impedances were close to the origin, while the low-frequency ones were farther away. The slope of the nearly straight section reflects the diffusion coefficient of Li⁺ ions, and the steeper the slope, the higher the ionic conductivity of the electrolyte is. The maximum extent of the semicircle (formed after discharge) on the Re(Z) axis is related to the charge transfer resistance in the system: the smaller the semi-circle, the faster the charge transfer and the higher the power density are. The intercept of the impedance curve with the Re(Z) axis is the bulk resistivity in the system (not discussed here). The charge transfer was fastest in the LiBF₄ and LiClO₄ electrolytes, while it was much slower in the LiPF₆ and LiBOB electrolytes. These observations are in agreement with the measured power densities discussed above.

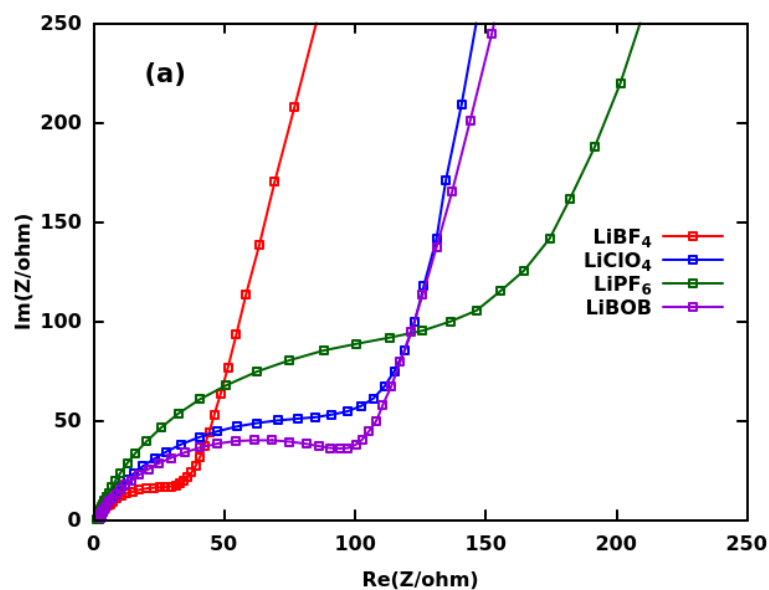


Figure 7. Cont.

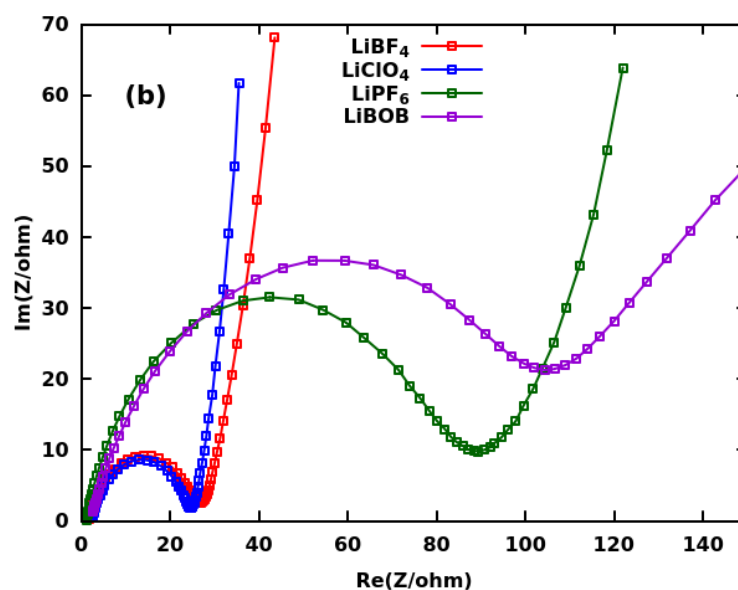


Figure 7. Impedance (Z) of Li- CF_x cells with 1 M LiBF_4 , LiClO_4 , LiPF_6 , and LiBOB electrolytes before (Panel a) and 1 h after (Panel b) full discharge at a 0.5 C rate. The electrolyte solvent was PC:DME:DOL(1:1:1).

The semicircles of the impedance data are less complete before discharge than after discharge. The more complete semicircle is typically a sign of the formation of a solid electrolyte interphase (SEI). Interestingly, the charge transfer resistance of the LiClO_4 electrolyte decreased greatly after the SEI formation and became about the same as that of LiBF_4 . This suggests that these latter two electrolytes may form similar SEIs on the anode and their SEIs may be very different from the SEIs of the LiPF_6 and LiBOB electrolytes. References [53,54] suggested that DOL polymerizes in the presence of suitable catalysts, such as Lewis acids, and this polymerization brings advantages for the formation of a stable SEI. Indeed, LiBF_4 can dissociate to LiF and BF_3 , and BF_3 is a Lewis acid, capable of initiating the polymerization of DOL even before discharge. On the other hand, LiClO_4 appears to be able to cause a similar effect during discharge. LiClO_4 is a well-known oxidation agent and a mild Lewis acid. It may release an oxygen radical during the discharge of the battery, while LiClO_3 would form and DOL would polymerize. Similar to the polymerization of DOL, the polymerization of the cyano group side-chains of the PAN can happen through the same effects and contributed to the reduced charge transfer resistance in the presence of the LiBF_4 and LiClO_4 electrolytes. The polymerization of the cyano group side-chains of the PAN resulted in a continuous $-\text{C}=\text{N}-$ conjugated pi-electron system, which likely improves the electronic conductivity in the system. Furthermore, the strands of the PAN can potentially also serve as ion conduction channels in the cathode based on the well-known property of PAN to form solid (gel) polymer electrolytes with high ionic conductivity [59,60].

Before discharge, the slope of the nearly straight section of the impedance curves was about the same for LiBF_4 , LiClO_4 , and LiBOB , while it was less steep for LiPF_6 . After discharge, the slope of LiClO_4 was the steepest, closely followed by LiBF_4 , while LiPF_6 was even less steep and LiBOB was the least steep one by far. Our current interpretation of these trends is that a fraction of the Li^+ ions of the electrolyte becomes immobilized during the SEI formation and the Li^+ concentration in the electrolyte decreases to a varying degree. Based on the trends of the slopes at a rate of 0.5C, the smallest amount of immobilized Li^+ may occur in LiClO_4 and LiBF_4 , while much more Li^+ may be immobilized in LiPF_6 and even more in LiBOB . This observation suggests that the anions of the latter two electrolytes may react with the PAN or CF_x during discharge and form discharge products that immobilize a fraction of the Li^+ ions of the electrolyte.

One possible reaction between LiPF_6 and PAN may be based on the chelation of PF_5 by the cyano groups of PAN. Similar chelation reactions of PF_5 through P-N bond and ring formation are well known [61]. In this process, the PF_5 would be derived from the dissociation of LiPF_6 to LiF and PF_5 . This chelation is more likely to happen during discharge when the N atoms of PAN may become more negatively charged and become more nucleophilic.

The immobilization of some Li^+ in the LiBOB electrolyte may be a result of a similar chelation around the B atom, whereby one oxalate ion is exchanged with two cyanide-ion-like units and Li-oxalate is precipitated. The cyanide-ion-like units may form from the cyano groups of PAN during discharge. The hydrolysis of LiBOB to boric and oxalic acids and their Li salts happens in a similar way with the involvement of hydroxide ions (instead of cyanide) [62].

In principle, the B atom of LiBF_4 can be chelated by PAN in a similar way; however, it seems to happen either to a smaller extent or it does not result in the immobilization of some Li^+ . The ClO_4^- ions cannot be chelated by PAN at all. Perhaps this is reflected by the high ionic conductivity in the batteries with the LiClO_4 electrolyte after discharge.

Further reactions are possible also between the electrolyte and CF_x in the presence of PAN or polymerized (in the cyano group side-chains) PAN (PPAN). For example, the oxalate groups of the BOB^- ions may participate in the Morita–Baylis–Hillman [63] reaction with CF_x in the presence of PPAN as a catalyst. A similar reaction was successfully carried out between NaOH and CF_x in the presence of a pyridine derivative base (4-Dimethylaminopyridine (DMAP)) and produced densely -OH-functionalized graphene and NaF [55]. PPAN shows structural similarity to the same pyridine derivative base and may play a similar catalytic role in the above-proposed reaction between LiBOB and CF_x .

Synchrotron XRD measurements were carried out on the discharged Li- CF_x cells with the PAN and PVDF binders in order to investigate the extent of the hypothetical inhibition of LiF crystallization by the PAN binder. The cells were discharged at a 0.5 C rate using 250 μm -thick cathodes. We found a large amount of crystalline LiF discharge product, as indicated in Figure 8. Our experience was contradictory to that of [37], which found no crystalline LiF in the XRD patterns of the discharged CF_x cathodes when a small concentration of BF_3 gas was used in the electrolyte. Therefore, we cannot confirm a similar degree of inhibition of LiF formation when the PAN binder is used. It is, however, possible that the inhibition caused by the PAN binder only slows down the LiF formation on a shorter time scale during discharge, and therefore, it could not be detected by our synchrotron XRD measurements about three weeks after the discharge. Consequently, the inhibition mechanism proposed by Jones and Hossain in [39] may still be valid.

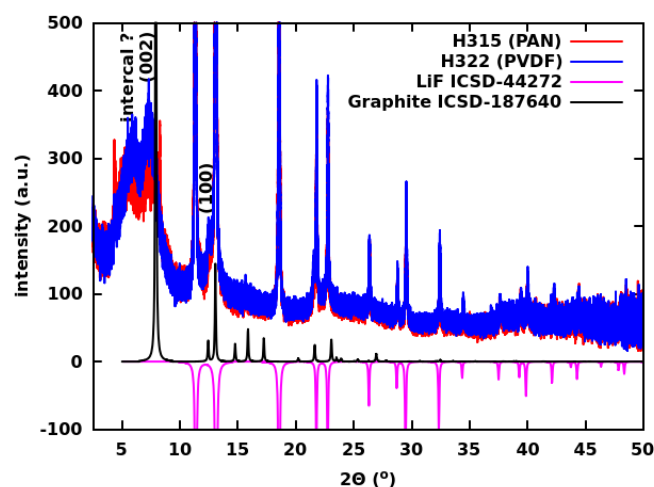


Figure 8. Synchrotron XRD patterns of the discharged cathodes of Li- CF_x cells with PAN and PVDF binders as compared to the patterns of graphite and LiF. The intensities of the LiF pattern are represented on the negative scale for clarity.

Note also that Jones and Hossain did not mention any electrolyte effects on their proposed inhibition mechanism of the LiF crystallization. Our study points out for the first time in the literature that a combined effect of the binder and the electrolyte can be a simple and robust means of greatly increasing the power density of Li-CF_x cells.

Further analysis of the XRD pattern of the discharge products also suggested that it may contain both turbostratic graphite (the broad peak at 7.4 degrees near the (002) reflection of graphite) and a first stage intercalation complex of graphite (the broad peak at 5.9 degrees). Unfortunately, we could not further investigate if these broad peaks might be associated with hard carbon, as suggested in [29].

Figure 9 shows the SEM image of a flake of CF_x after discharge at a 0.5 C rate. It seems nearby LiF crystals are placed along local strings. This arrangement of LiF crystals may indicate that the strands of PAN serve as nucleation centers for the crystallization of LiF. This observation is in agreement with the prediction of Jones and Hossain that certain polymers bind to LiF crystals and influence their growth [39]. Without PAN, LiF could nucleate at pores, clogging the transport routes of Li⁺ ions. On the one hand, it appears that PVDF or PTFE binders have a smaller complexation affinity to LiF and, therefore, can assist less in its nucleation [64,65]. On the other hand, the ability of PAN to complex and nucleate LiF depends greatly on the electrolyte, as shown above. Further note that, in our experience, the CF_x cathodes with the PAN binder appeared to stick better to the Al foil current collectors than with the PVDF binders after the discharge of the battery. This may perhaps indicate a significant difference in the distribution and size of LiF crystals in the presence of different binders.

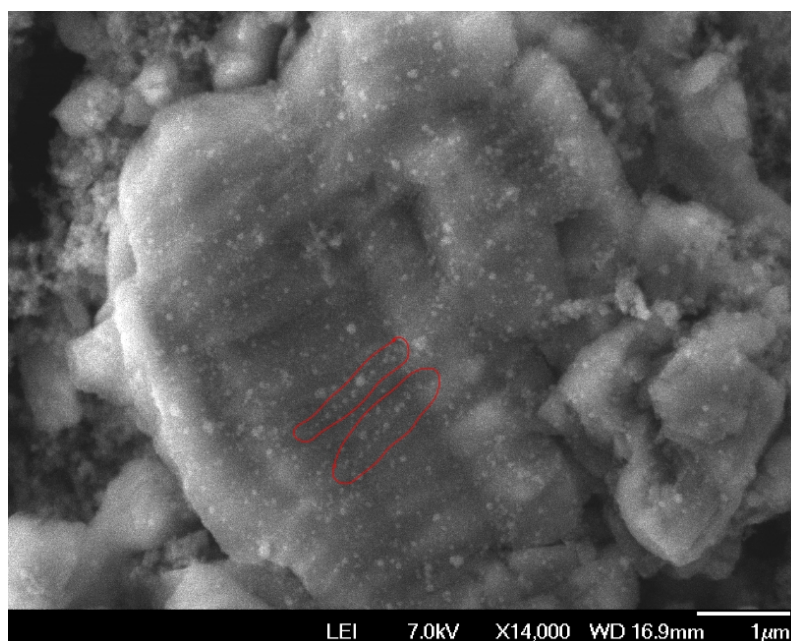


Figure 9. SEM image of a flake of CF_x after discharge at a 0.5 C rate. Bright spots indicate LiF crystals. The red encircled area highlights the arrangement of LiF crystals along a string.

The morphology of the cathodes after discharge (until the cut-off voltage of 1.5 V is reached) at different C-rates is shown in Figure 10 along with the EDS maps of the F and N atoms. It was assumed that the N atom contribution comes from the PAN only (the residual DMF should be of a negligible amount); therefore, the comparison of the F and N maps is informative about the relative locations of the C-F bonds or LiF crystals and PAN in the cathodes. The distribution of PAN in the cathode seemed to be sufficiently homogeneous before discharge. The same homogeneous distribution of PAN appeared to be present after discharge. It seemed PAN was located near where LiF was located. This observation further suggested that PAN may serve as a nucleation center for LiF crystal growth.

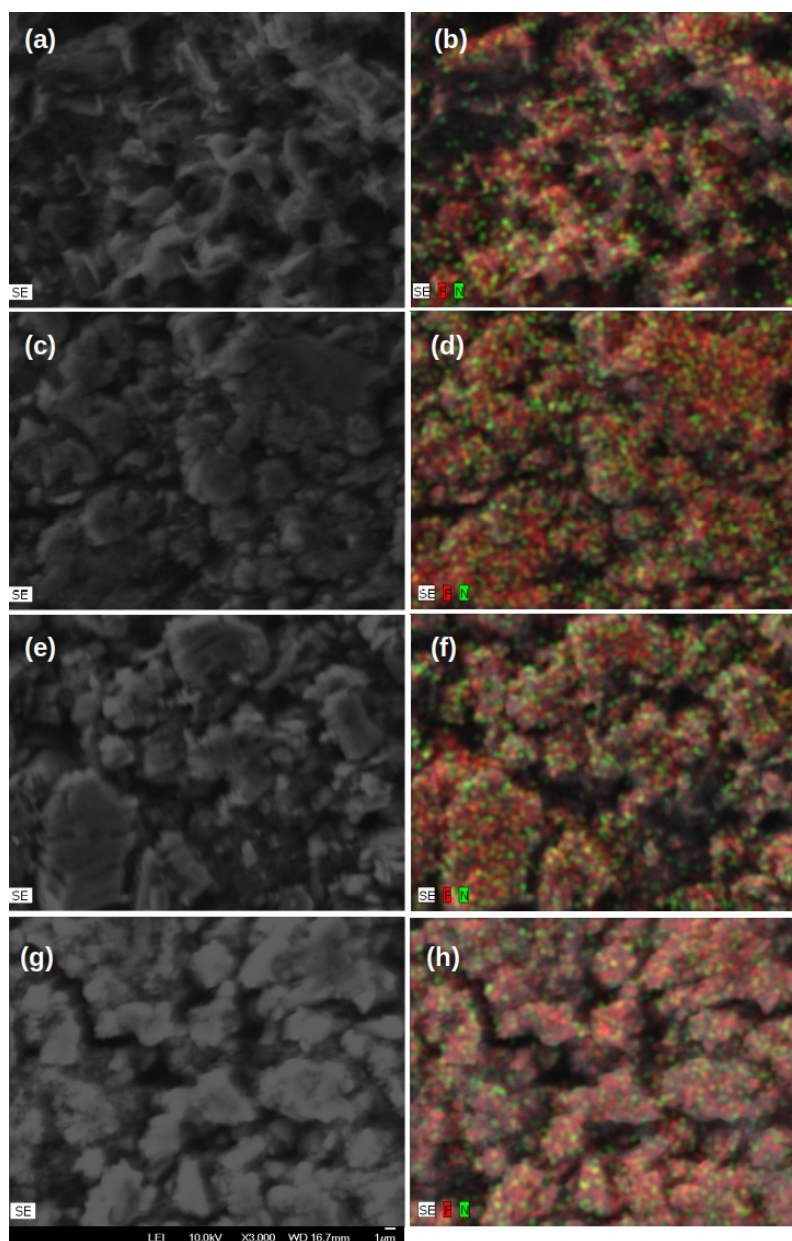
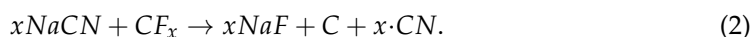


Figure 10. SEM images of CF_x cathodes (left panels) and the corresponding EDS maps of F (red) and N (green) atoms (right panels) after discharge at different C rates. The following C rates were studied: 0 (no discharge, Panels (a,b)); 0.5 (c,d); 10 (e,f); 30 (g,h).

The mechanistic origin of the observed combined binder and electrolyte effects on the power density is not clear yet. Several analogous reactions, however, point toward the electro-catalytic effect of PAN in the given circumstances. As PAN $((CH_2CH-CN)_x)$ has cyano (-CN) group side-chains, it is reasonable to assume that these -CN groups would be oxidized by CF_x in a similar manner to the oxidation of NaCN by CF_x [57]:



The resulting $\cdot CN$ radicals mostly dimerize to cyanogen (NC-CN) and then polymerize to paracyanogen $(CN)_{2n}$ [57] and, to a lesser extent, may covalently functionalize the graphene sheets [56]. In PAN, an oxidative effect by CF_x or by the electrolyte is expected to result in the polymerization of the -CN groups in the side-chains. Such a side-chain polymerization of PAN has been known for long as an effect of heating, and it results in pyridine-type rings and a ladder-type polymer [66].

We propose that the side-chain polymerized PAN (PPAN) functions as an electro-catalyst. The catalytic mechanism is depicted in Figure 11. PPAN and CF_x form a cyclo-adduct after the nucleophilic attack of PPAN on CF_x . This cyclo-adduct is the activated complex of the reaction mechanism. When the battery discharges, the cyclo-adduct is reduced and splits into a residual CF_x with a newly formed C=C double-bond and a recycled PPAN, while also LiF is formed.

The conjugated -C=N- pi-electron system in the side-chain of PPAN could potentially have a good electronic conductivity if the atoms in the -C=N- chain remain co-planar and sp^2 hybridized even in the activated complex. In this situation, the N atoms of the activated complex would carry a positive charge, which is counterbalanced by an electrolyte anion A^- , which is not covalently bound to PPAN. The F of the activated complex would precipitate as LiF (extracting Li from the electrolyte) as soon as the activated complex forms. Upon discharge, the activated complex would decompose to PPAN, a new C=C double-bond in the residual CF_x , and a restored LiA electrolyte salt. This alternative model is shown in Figure 12. In this situation, the PPAN may play three roles: it is an electro-catalyst and a conductor of electrons and ions to the activated complex.

The catalytic cycle can be active as long as there is a supply of Li and C-F bonds. It seems that PPAN must move on the surface of CF_x in order to harvest new C-F bonds. This motion of PPAN can be beneficial for opening up the space between stacked CF_x layers. This may be the reason that the catalytic effect works quite well even on non-ultrasonicated CF_x . The PAN/PPAN catalyst may be poisoned by certain electrolytes that react with it or with CF_x . As discussed above, LiBOB and LiPF_6 appear to be such electrolytes. Since the PVDF and PTFE binders are not reactive with CF_x , they cannot provide catalytic effects. Therefore, the proposed catalytic mechanism can account for all the observed phenomena.

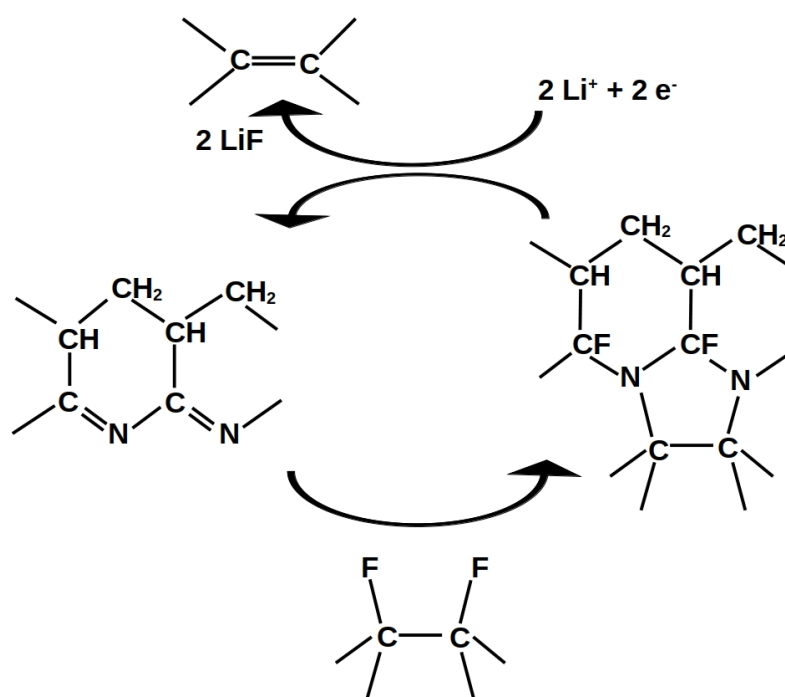


Figure 11. The proposed electro-catalytic action of the PAN binder on CF_x during the discharge of the Li- CF_x cell. PAN is represented by its side-chain polymerized form (PPAN).

Conflicts of Interest: The authors declare no conflict of interest. The funders had no role in the design of the study; in the collection, analyses, or interpretation of the data; in the writing of the manuscript; nor in the decision to publish the results.

References

1. Trahey, L.; Brushett, F.R.; Balsara, N.P.; Ceder, G.; Cheng, L.; Chiang, Y.M.; Hahn, N.T.; Ingram, B.J.; Minter, S.D.; Moore, J.S.; et al. Energy storage emerging: A perspective from the Joint Center for Energy Storage Research. *Proc. Natl. Acad. Sci. USA* **2020**, *117*, 12550–12557. [[CrossRef](#)]
2. Yang, X.G.; Liu, T.; Ge, S.; Rountree, E.; Wang, C.Y. Challenges and key requirements of batteries for electric vertical takeoff and landing aircraft. *Joule* **2021**, *5*, 1644–1659. [[CrossRef](#)]
3. Bills, A.; Sripad, S.; Fredericks, W.L.; Singh, M.; Viswanathan, V. Performance metrics required of next-generation batteries to electrify commercial aircraft. *ACS Energy Lett.* **2020**, *5*, 663–668. [[CrossRef](#)]
4. Krause, F.; Ruiz, J.; Jones, S.; Brandon, E.; Darcy, E.; Iannello, C.; Bugga, R. Performance of commercial Li-ion cells for future NASA missions and aerospace applications. *J. Electrochem. Soc.* **2021**, *168*, 040504. [[CrossRef](#)]
5. Krause, F.C.; Jones, J.P.; Jones, S.C.; Pasalic, J.; Billings, K.J.; West, W.C.; Smart, M.C.; Bugga, R.V.; Brandon, E.J.; Destephen, M. High specific energy lithium primary batteries as power sources for deep space exploration. *J. Electrochem. Soc.* **2018**, *165*, A2312. [[CrossRef](#)]
6. Ndzebet, E.; Destephen, M.; Zhang, D.; Darch, D. High Power and High Rate Li/CF_x-MnO₂ Pouch Cell Hybrid Technology. In Proceedings of the 48th Power Sources Conference, Denver, CO, USA, 11–14 June 2018; pp. 558–561.
7. Greatbatch, W.; Holmes, C.; Takeuchi, E.; Ebel, S. Lithium/carbon monofluoride (Li/CF_x): A new pacemaker battery. *Pacing Clin. Electrophysiol.* **1996**, *19*, 1836–1840. [[CrossRef](#)]
8. Ruff, O.; Bretschneider, O. Die Reaktionsprodukte der verschiedenen Kohlenstoffformen mit Fluor II (Kohlenstoff-monofluorid). *Z. Anorg. Allg. Chem.* **1934**, *217*, 1–18. [[CrossRef](#)]
9. Rüdorff, W.; Rüdorff, G. Zur Konstitution des Kohlenstoff-Monofluorids. *Z. Anorg. Chem.* **1947**, *253*, 281–296. [[CrossRef](#)]
10. Watanabe, N.; Fukuda, M. Primary Cell for Electric Batteries. U.S. Patent 3,536,532, 27 October 1970.
11. Watanabe, K.; Fukuda, M. High Energy Density Battery. U.S. Patent 3,700,502, 24 October 1972.
12. Fukuda, M.; Iijima, T.; Toyoguchi, Y. Active Material for Positive Electrode of Battery. U.S. Patent 4,271,242, 2 June 1981.
13. Sharma, N.; Dubois, M.; Guérin, K.; Pischedda, V.; Radescu, S. Fluorinated (Nano) Carbons: CF_x Electrodes and CF_x-Based Batteries. *Energy Technol.* **2021**, *9*, 2000605. [[CrossRef](#)]
14. Ahmad, Y.; Batisse, N.; Chen, X.; Dubois, M. Preparation and Applications of Fluorinated Graphenes. *C* **2021**, *7*, 20. [[CrossRef](#)]
15. Wang, D.; Wang, G.; Zhang, M.; Cui, Y.; Yu, J.; Shi, S. Composite cathode materials for next-generation lithium fluorinated carbon primary batteries. *J. Power Sources* **2022**, *541*, 231716. [[CrossRef](#)]
16. Groult, H.; Tressaud, A. Use of inorganic fluorinated materials in lithium batteries and in energy conversion systems. *Chem. Commun.* **2018**, *54*, 11375–11382. [[CrossRef](#)] [[PubMed](#)]
17. Zhang, Q.; Takeuchi, K.J.; Takeuchi, E.S.; Marschilok, A.C. Progress towards high-power Li/CF_x batteries: Electrode architectures using carbon nanotubes with CF_x. *Phys. Chem. Chem. Phys.* **2015**, *17*, 22504–22518. [[CrossRef](#)] [[PubMed](#)]
18. Chen, P.; Jiang, C.; Jiang, J.; Zou, J.; Ran, Q.; Wang, X.; Niu, X.; Wang, L. Fluorinated Carbons as Rechargeable Li-Ion Battery Cathodes in the Voltage Window of 0.5–4.8 V. *ACS Appl. Mater. Interfaces* **2021**, *13*, 30576–30582. [[CrossRef](#)]
19. Liu, W.; Li, H.; Xie, J.Y.; Fu, Z.W. Rechargeable room-temperature CF_x-sodium battery. *ACS Appl. Mater. Interfaces* **2014**, *6*, 2209–2212. [[CrossRef](#)]
20. Whittingham, M.S. Mechanism of reduction of the fluorographite cathode. *J. Electrochem. Soc.* **1975**, *122*, 526. [[CrossRef](#)]
21. Watanabe, N.; Nakajima, T.; Hagiwara, R. Discharge reaction and overpotential of the graphite fluoride cathode in a nonaqueous lithium cell. *J. Power Sources* **1987**, *20*, 87–92. [[CrossRef](#)]
22. Watanabe, N.; Hagiwara, R.; Nakajima, T.; Touhara, H.; Ueno, K. Solvents effects on electrochemical characteristics of graphite fluoride—lithium batteries. *Electrochim. Acta* **1982**, *27*, 1615–1619. [[CrossRef](#)]
23. Jang, B.Z.; Liu, C.; Neff, D.; Yu, Z.; Wang, M.C.; Xiong, W.; Zhamu, A. Graphene surface-enabled lithium ion-exchanging cells: next-generation high-power energy storage devices. *Nano Lett.* **2011**, *11*, 3785–3791. [[CrossRef](#)]
24. Liu, C.; Zhamu, A.; Neff, D.; Jang, B.Z. Lithium Super-Battery with a Functionalized Nano Graphene Cathode. U.S. Patent 8,795,899, 5 August 2014
25. Kim, H.; Park, K.Y.; Hong, J.; Kang, K. All-graphene-battery: Bridging the gap between supercapacitors and lithium ion batteries. *Sci. Rep.* **2014**, *4*, 5278. [[CrossRef](#)]
26. Kim, H.; Park, Y.U.; Park, K.Y.; Lim, H.D.; Hong, J.; Kang, K. Novel transition-metal-free cathode for high energy and power sodium rechargeable batteries. *Nano Energy* **2014**, *4*, 97–104. [[CrossRef](#)]
27. Kornilov, D.; Penki, T.R.; Cheglakov, A.; Aurbach, D. Li/graphene oxide primary battery system and mechanism. *Battery Energy* **2022**, *1*, 20210002. [[CrossRef](#)]
28. Zhang, S.S.; Foster, D.; Wolfenstine, J.; Read, J. Electrochemical characteristic and discharge mechanism of a primary Li/CF_x cell. *J. Power Sources* **2009**, *187*, 233–237. [[CrossRef](#)]

29. Sayahpour, B.; Hirsh, H.; Bai, S.; Schorr, N.B.; Lambert, T.N.; Mayer, M.; Bao, W.; Cheng, D.; Zhang, M.; Leung, K.; et al. Revisiting discharge mechanism of CF_x as a high energy density cathode material for lithium primary battery. *Adv. Energy Mater.* **2022**, *12*, 2103196. [[CrossRef](#)]
30. Yazami, R.; Hamwi, A.; Guérin, K.; Ozawa, Y.; Dubois, M.; Giraudet, J.; Masin, F. Fluorinated carbon nanofibres for high energy and high power densities primary lithium batteries. *Electrochem. Commun.* **2007**, *9*, 1850–1855. [[CrossRef](#)]
31. Lam, P.; Yazami, R. Physical characteristics and rate performance of (CF_x)_n (0.33 < x < 0.66) in lithium batteries. *J. Power Sources* **2006**, *153*, 354–359.
32. Luo, Z.; Wang, X.; Chen, D.; Chang, Q.; Xie, S.; Ma, Z.; Lei, W.; Pan, J.; Pan, Y.; Huang, J. Ultrafast Li/fluorinated graphene primary batteries with high energy density and power density. *ACS Appl. Mater. Interfaces* **2021**, *13*, 18809–18820. [[CrossRef](#)] [[PubMed](#)]
33. Dai, Y.; Cai, S.; Wu, L.; Yang, W.; Xie, J.; Wen, W.; Zheng, J.C.; Zhu, Y. Surface modified CF_x cathode material for ultrafast discharge and high energy density. *J. Mater. Chem. A* **2014**, *2*, 20896–20901. [[CrossRef](#)]
34. Peng, C.; Kong, L.; Li, Y.; Fu, H.; Sun, L.; Feng, Y.; Feng, W. Fluorinated graphene nanoribbons from unzipped single-walled carbon nanotubes for ultrahigh energy density lithium-fluorinated carbon batteries. *Sci. China Mater.* **2021**, *64*, 1367–1377. [[CrossRef](#)]
35. Jiang, S.; Huang, P.; Lu, J.; Liu, Z. The electrochemical performance of fluorinated ketjenblack as a cathode for lithium/fluorinated carbon batteries. *RSC Adv.* **2021**, *11*, 25461–25470. [[CrossRef](#)]
36. Wang, K.; Feng, Y.; Kong, L.; Peng, C.; Hu, Y.; Li, W.; Li, Y.; Feng, W. The fluorination of boron-doped graphene for CF_x cathode with ultrahigh energy density. *Energy Environ. Mater.* **2022**, e12437. [[CrossRef](#)]
37. Li, Q.; Xue, W.; Sun, X.; Yu, X.; Li, H.; Chen, L. Gaseous electrolyte additive BF₃ for high-power Li/CF_x primary batteries. *Energy Storage Mater.* **2021**, *38*, 482–488. [[CrossRef](#)]
38. Rangasamy, E.; Li, J.; Sahu, G.; Dudney, N.; Liang, C. Pushing the theoretical limit of Li-CF_x batteries: A tale of bifunctional electrolyte. *J. Am. Chem. Soc.* **2014**, *136*, 6874–6877. [[CrossRef](#)] [[PubMed](#)]
39. Jones, S.C.; Hossain, S. Polymer Materials as Binder for a CF_x Cathode, . U.S. Patent Application 13/010,431, 28 July 2011.
40. Németh, K. Materials design by quantum-chemical and other theoretical/computational means: Applications to energy storage and photoemissive materials. *Int. J. Quantum Chem.* **2014**, *114*, 1031–1035. [[CrossRef](#)]
41. Zhang, F.; Németh, K.; Bareño, J.; Dogan, F.; Bloom, I.D.; Shaw, L.L. Experimental and theoretical investigations of functionalized boron nitride as electrode materials for Li-ion batteries. *RSC Adv.* **2016**, *6*, 27901–27914. [[CrossRef](#)]
42. Németh, K. Simultaneous oxygen and boron trifluoride functionalization of hexagonal boron nitride: A designer cathode material for energy storage. *Theor. Chem. Accounts* **2018**, *137*, 157. [[CrossRef](#)]
43. Németh, K. Radical anion functionalization of two-dimensional materials as a means of engineering simultaneously high electronic and ionic conductivity solids. *Nanotechnology* **2021**, *32*, 245709. [[CrossRef](#)]
44. Nemeth, K. Functionalized Boron Nitride Materials as Electroactive Species in Electrochemical Energy Storage Devices. U.S. Patent 10,693,137, 23 June 2020.
45. Nemeth, K. Radical Anion Functionalization of Two-Dimensional Materials. U.S. Patent 11,453,596 B2, 7 September 2022 .
46. Marshall, J.E.; Zhenova, A.; Roberts, S.; Petchey, T.; Zhu, P.; Dancer, C.E.; McElroy, C.R.; Kendrick, E.; Goodship, V. On the solubility and stability of polyvinylidene fluoride. *Polymers* **2021**, *13*, 1354. [[CrossRef](#)]
47. Zor, C.; Subaşı, Y.; Hacıu, D.; Somer, M.; Afyon, S. Guide to water free lithium bis (oxalate) borate (LiBOB). *J. Phys. Chem. C* **2021**, *125*, 11310–11317. [[CrossRef](#)]
48. Zhang, M.; Ma, Y.; Zhu, Y.; Che, J.; Xiao, Y. Two-dimensional transparent hydrophobic coating based on liquid-phase exfoliated graphene fluoride. *Carbon* **2013**, *63*, 149–156. [[CrossRef](#)]
49. Zeng, X.; Peng, Y.; Yu, M.; Lang, H.; Cao, X.; Zou, K. Dynamic sliding enhancement on the friction and adhesion of graphene, graphene oxide, and fluorinated graphene. *ACS Appl. Mater. Interfaces* **2018**, *10*, 8214–8224. [[CrossRef](#)] [[PubMed](#)]
50. Huo, H. High Energy High Power Primary Lithium Batteries with Graphite Fluoride and Functionalized Boron Nitride Cathodes. Master's Thesis, Illinois Institute of Technology, Chicago, IL, USA , 2022.
51. Tatagari, V.R. A Functionalized 2D Boron Nitride Electrode for Rechargeable Batteries. Master's Thesis, Illinois Institute of Technology, Chicago, IL, USA, 2021.
52. Li, Y.Y.; Liu, C.; Chen, L.; Wu, X.Z.; Zhou, P.F.; Shen, X.Y.; Zhou, J. Multi-layered fluorinated graphene cathode materials for lithium and sodium primary batteries. *Rare Metals* **2022**, *42*, 940–953. [[CrossRef](#)]
53. Zhao, Q.; Liu, X.; Zheng, J.; Deng, Y.; Warren, A.; Zhang, Q.; Archer, L. Designing electrolytes with polymerlike glass-forming properties and fast ion transport at low temperatures. *Proc. Natl. Acad. Sci. USA* **2020**, *117*, 26053–26060. [[CrossRef](#)] [[PubMed](#)]
54. Ma, L.; Kim, M.S.; Archer, L.A. Stable artificial solid electrolyte interphases for lithium batteries. *Chem. Mater.* **2017**, *29*, 4181–4189. [[CrossRef](#)]
55. Bai, L.; Xu, Y.; Liu, A.; Dong, L.; Zhang, K.; Li, W.S.; Zhao, F.G. Unusual graphite fluoride hydrolysis toward unconventional graphene oxide for high-performance supercapacitors and Li-ion batteries. *Chem. Eng. J.* **2022**, *434*, 134639. [[CrossRef](#)]
56. Bakandritsos, A.; Pykal, M.; Błoński, P.; Jakubec, P.; Chronopoulos, D.D.; Poláková, K.; Georgakilas, V.; Čépe, K.; Tomanec, O.; Ranc, V.; et al. Cyanographene and graphene acid: Emerging derivatives enabling high-yield and selective functionalization of graphene. *ACS Nano* **2017**, *11*, 2982–2991. [[CrossRef](#)]

57. Siedle, A.; Losovyj, Y.; Stein, B.D.; Pink, M.; Werner-Zwanziger, U. Cyanographite. *J. Phys. Chem. C* **2022**, *126*, 3001–3008. [[CrossRef](#)]
58. Pang, C.; Ding, F.; Sun, W.; Liu, J.; Hao, M.; Wang, Y.; Liu, X.; Xu, Q. A novel dimethyl sulfoxide/1,3-dioxolane based electrolyte for lithium/carbon fluorides batteries with a high discharge voltage plateau. *Electrochim. Acta* **2015**, *174*, 230–237. [[CrossRef](#)]
59. Watanabe, M.; Kanba, M.; Nagaoka, K.; Shinohara, I. Ionic conductivity of hybrid films composed of polyacrylonitrile, ethylene carbonate, and LiClO₄. *J. Polym. Sci. Polym. Phys. Ed.* **1983**, *21*, 939–948. [[CrossRef](#)]
60. Chen, H.; Lin, F.; Chen, C. Polyacrylonitrile electrolytes 1. A novel high-conductivity composite polymer electrolyte based on PAN, LiClO₄ and α -Al₂O₃. *Solid State Ionics* **2002**, *150*, 327–335. [[CrossRef](#)]
61. Wong, C.Y.; Kennepohl, D.K.; Cavell, R.G. Neutral six-coordinate phosphorus. *Chem. Rev.* **1996**, *96*, 1917–1952. [[CrossRef](#)]
62. Amereller, M.; Multerer, M.; Schreiner, C.; Lodermeier, J.; Schmid, A.; Barthel, J.; Gores, H.J. Investigation of the hydrolysis of lithium bis [1,2-oxalato (2-)-O, O'] borate (LiBOB) in water and acetonitrile by conductivity and NMR measurements in comparison to some other borates. *J. Chem. Eng. Data* **2009**, *54*, 468–471. [[CrossRef](#)]
63. Wei, Y.; Shi, M. Recent Advances in Organocatalytic Asymmetric Morita–Baylis–Hillman/aza-Morita–Baylis–Hillman Reactions. *Chem. Rev.* **2013**, *113*, 6659–6690. [[CrossRef](#)] [[PubMed](#)]
64. De Yoreo, J.J.; Vekilov, P.G. Principles of crystal nucleation and growth. *Rev. Mineral. Geochem.* **2003**, *54*, 57–93. [[CrossRef](#)]
65. Vekilov, P.G. The two-step mechanism of nucleation of crystals in solution. *Nanoscale* **2010**, *2*, 2346–2357. [[CrossRef](#)]
66. Chung, T.C.; Schlesinger, Y.; Etemad, S.; Macdiarmid, A.; Heeger, A. Optical studies of pyrolyzed polyacrylonitrile. *J. Polym. Sci. Polym. Phys. Ed.* **1984**, *22*, 1239–1246. [[CrossRef](#)]

Disclaimer/Publisher's Note: The statements, opinions and data contained in all publications are solely those of the individual author(s) and contributor(s) and not of MDPI and/or the editor(s). MDPI and/or the editor(s) disclaim responsibility for any injury to people or property resulting from any ideas, methods, instructions or products referred to in the content.